CONFERENCE PRE-PRINT

PREDICTIVE STUDY OF NON-AXISYMMETRIC NEUTRAL BEAM ION LOSS ON THE UPGRADED KSTAR PLASMA-FACING COMPONENTS

T. MOON
Ulsan National Institute of Science and Technology
Ulsan, Republic of Korea

T. RHEE
Korea Institute of Fusion Energy
Daejeon, Republic of Korea

J.-M. KWON
Korea Institute of Fusion Energy
Daejeon, Republic of Korea

Y.-M. JEON
Korea Institute of Fusion Energy
Daejeon, Republic of Korea

*E.S. YOON
Ulsan National Institute of Science and Technology
Ulsan, Republic of Korea
*Corresponding Author: esyoon@unist.ac.kr

Abstract

Non-axisymmetric neutral-beam-injection (NBI)-induced ion loss patterns are found on KSTAR's upgraded tungsten plasma-facing components (PFCs). Unfolded divertor and poloidal limiter (PL) maps show diagonal, band-shaped wetted areas produced by the combined poloidal-turn and toroidal drift of fast ions; localized peaks arise at protruding surfaces and the leading edges of the tungsten divertor. To evaluate where and how such loss occurs, we adopt a CAD-to-simulation-ready KSTAR PFC surface mesh and a 3D collision-detection routine. NBI simulation parameter scans with NuBDeC code vary KSTAR NB system 1 sources (NB1-A/B/C), beam energy (60–100 keV), plasma current I_p (0.50/0.75/1.00 MA), poloidal beta β_p (1.0/2.0), and the separatrix strike-point location (outer/central divertor). Along the simulation setups of the parameter scan, decreasing energy from 100 to 60 keV narrows poloidal wetting and reduces both the maximum heat flux (~75-80%) and the deposited-power fraction (~90-95%); deposition close to SOL region (NB1-C), larger β_p, and lower I_p increase ion losses, while a strike-point shift from outer to central divertor broadens wetting and can drive inboard-limiter hits. The results can provide a systematic approach for optimizing NBI configuration—selecting source, energy, I_p-β_p operating windows, and strike-point placement—to avoid localized loading on the W-divertor during KSTAR operation. Moreover, the resulting heat flux datasets are loadable on the V-KSTAR platform and are intended for further use in synthetic diagnostics and integrated simulation, providing engineering-level fidelity and seamless geometrical context on which the data can be mapped.

1. INTRODUCTION

Neutral beam injection (NBI) generates high-energy ions in fusion plasmas, and a fraction of these fast ions can escape confinement and collide with plasma-facing components (PFCs). These lost fast ions deposit heat flux on walls, limiters, and divertors, potentially causing localized overheating. Multiple studies have investigated the causes of this overheating with NBI heating simulations [1, 2, 3, 4, 5]. In particular, KSTAR researches have examined NB ion loss using both numerical methods and experiments [6, 7, 8], and one identified cause of the observed overheating is NBI-induced NB ion loss [6, 9]. This motivates quantitative modeling of fast-ion loss and the associated wall heat loads to ensure PFC integrity and to enable safe and efficient NBI operation.

Accurate modeling of fast-ion loss and the resulting heat loads requires wall geometry whose fidelity meets with the target spatial resolution. Early studies commonly adopted simplified and axisymmetric (2D poloidal) vessel models [9, 10], whereas recent work incorporates full 3D CAD geometry to obtain higher-fidelity predictions [3, 11]. In this context, the NB deposition and orbit-following simulation code (NuBDeC) [6] has been equipped with

realistic wall geometry and collision-detection capability in 3D space [12], enabling direct computation of fast-ion impacts on detailed PFC features where non-axisymmetric loading is expected.

Many researchers have employed CAD-to-simulation modules to introduce engineering-level-fidelity geometry into the simulation environment. This enables deployment into synthetic diagnostics [13, 14, 15, 16] and supports integrated modeling frameworks [17, 18]. Furthermore, considering real-world geometry in simulation provides a systematic approach to detect defects which are subtle, non-trivial, yet critical to system integrity [19, 20]. It connects model predictions to actionable engineering safeguards.

This research models NB ion loss for KSTAR PFCs—including the newly upgraded tungsten divertor—using NuBDeC. Across a parameter scan covering beam energies, beam sources, and magnetic equilibria, we identify robust non-axisymmetric loss patterns on PFCs. An inclined non-axisymmetric heat flux distribution is shown, and heat-flux concentration is captured on engineering-level details such as leading edges and local protrusions. Translations, magnification/shrinkage, and shifts of the peak heat flux distribution are described and linked to fast-ion drifts; within the NuBDeC simulation parameter scan the loss is expected to vary with source geometry, energy, and equilibrium. The results can provide a systematic approach for optimizing NBI configuration to avoid localized loading on KSTAR's W-divertor, suggesting NBI settings that mitigate NBI-induced fast-ion wall loads.

2. METHOD

2.1. Overall analysis framework

The analysis comprises three sequential simulation and post-processing steps: (i) NB ionization modeling, (ii) orbit following with collision detection against the 3D wall geometry, and (iii) calculation and analysis of heat flux distribution. The first two steps model the complete lifetime of wall-colliding NB ions. Subsequently, heat flux from NBI-induced ion loss is calculated based on the computed wall collisions. The maximum heat flux values and power deposition are then analyzed for each categorized PFC region.

2.2. Geometry-based analysis

2.2.1. CAD-to-simulation-ready mesh and collision detection in 3D space

At each NuBDeC simulation time step, NB ion loss is captured by detecting collisions between KSTAR PFC surfaces and path segments formed by straight lines connecting NB ion positions at the previous and current time steps. This study employs an unstructured mesh to accurately represent the CAD geometry of KSTAR PFC surfaces. Unlike structured meshes comprising regularly arranged cells (typically quadrilaterals in 2D), unstructured meshes provide superior flexibility in capturing intricate geometries such as KSTAR PFC components. To minimize computational cost, efficient algorithms for unstructured meshes are implemented in the NuBDeC code.

The collision detection algorithms utilized for the broad and narrow phases are described in Reference [21]. At each time step, straight-segment ion paths are tested for wall intersection using a two-stage broad/narrow pipeline: tri-oval culling combined with uniform-grid hashing to retrieve nearby triangles (broad phase), followed by ray casting for exact segment-triangle intersection (narrow phase). This approach minimizes pairwise tests while preserving geometric fidelity. The complete collision detection process for NuBDeC, including algorithms employed in each phase, is detailed in Reference [12].

2.2.2. KSTAR PFC mesh

The unstructured mesh used for collision detection is constructed through triangular tessellation (376,747 triangles, each approximately 5 cm in size) over the defeatured PFC geometry. In the tessellation process, the mesh is built exclusively on PFC surfaces and leading edges where NB ion collisions are expected. Fig. 1 displays the NuBDeC mesh for this study obtained through these procedures.

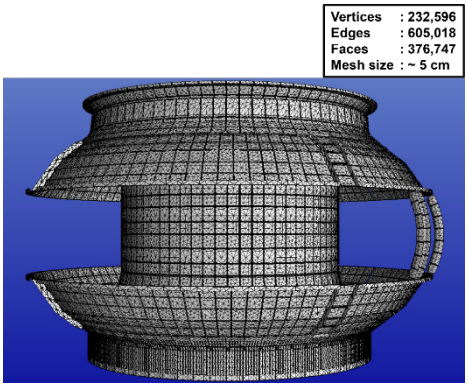

FIG. 1. A mesh for the KSTAR PFC geometry used in the 3D collision detection to calculate the positions of NB ion loss.

2.3. NBI heating modeling with NuBDeC

NB ionization is modeled using the random threshold method with a bi-Gaussian beam source [6]. The NB source configuration in simulations aligns with specifications in Reference [22]. For particle orbits, the full Lorentz orbit including gyration is employed for loss detection on PFC surfaces. The Lorentz orbit ($\frac{d\vec{x}}{dt} = \vec{v}$, $\frac{d\vec{v}}{dt} = \frac{q}{m}(\vec{v} \times \vec{B})$) is calculated using the Runge-Kutta fourth-order method. $\vec{x}$ is position, $\vec{v}$ is velocity, t is time. $\frac{q}{m}$ is the ion charge-to-mass ratio of the target ion, $\vec{B}$ is the magnetic equilibrium field. $\vec{E} = 0$ is assumed.

Along each orbit, when particles collide with the wall, the collision event is recorded as a loss in the respective PFC region categorized as divertor, PL, or others, as described in Fig. 2. Specifically, when the i-th sample ion particle collides with the j-th mesh element, its kinetic energy is deposited on that element. For a beam injection duration of Δt, the NBI-induced ion loss heat flux Γ_j is assigned to each j-th element according to: $\Gamma_j = \sum_i \frac{\omega E_i}{A_j \Delta t}$, where ω is the particle weight, E_i is the kinetic energy, and A_j is the element area.

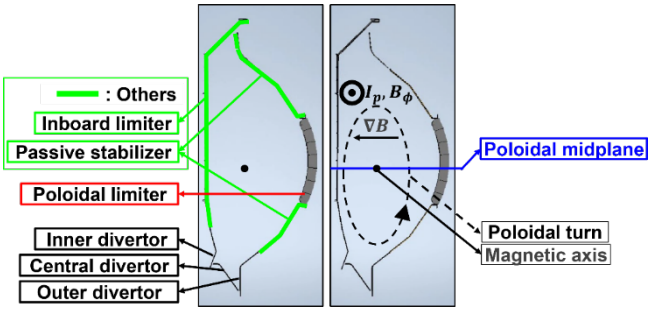

FIG. 2. Toroidal cross section of KSTAR PFC surfaces illustrating the poloidal turn, poloidal midplane, and the following PFC regions, used for categorizing the simulation results: divertor, PL, and others, which include the plasma-facing surface of passive stabilizer and inboard limiter.

2.4. Simulation setup

The analysis focuses on NB1 (sources A/B/C at KSTAR port L; tangential radii 1.486, 1.72, 1.245 m, respectively) [22]. The parameter scan includes NB1 sources (A/B/C), beam energies of 60-100 keV, plasma current $I_p \in \{0.50, 0.75, 1.00\}$ MA, and poloidal beta $\beta_p \in \{1.0, 2.0\}$. An additional equilibrium configuration places the outer separatrix strike point on the central divertor. Magnetic ripple effects are neglected (approximately 0.04% amplitude). Each setup tracks 2.4×10^6 Monte Carlo ions. Equilibria are summarized in Table 1 and Fig. 3-i. For beam deposition calculations, electron density and temperature profiles are configured as shown in Fig. 3-ii, representing typical KSTAR H-mode profiles.

TABLE 1. Plasma current (I_p), poloidal beta (β_p), and the strike point position of the outer separatrix leg for each magnetic equilibrium illustrated in Fig. 3-i.

Equilibrium case	I_p [MA]	β_p	Strike point position
(I)	1.00	1.0	Outer
(II)	1.00	2.0	Outer
(III)	0.75	1.0	Outer
(IV)	0.75	2.0	Outer
(V)	0.50	1.0	Outer
(VI)	0.50	2.0	Outer
(VII)	1.00	1.0	Central

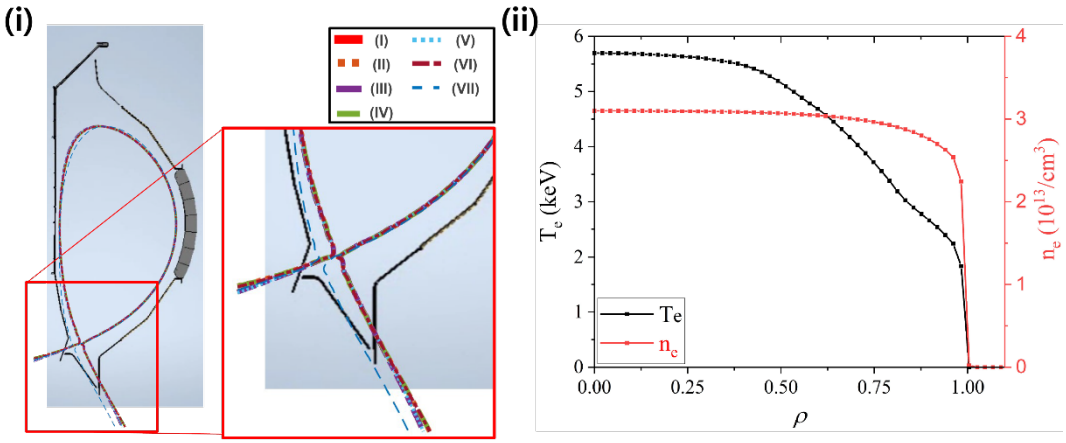

FIG. 3. (i) Toroidal cross section of magnetic separatrices for seven magnetic equilibria (Table 1) in the NuBDeC simulation parameter scan. Equilibrium case I is the reference setup. (ii) One-dimensional profiles of electron temperature (T_e) and density (N_e) over.

3. RESULTS

3.1. Non-axisymmetric heat flux distribution

In the reference case (100 keV, NB1-C; I_p= 1.00 MA, β_p= 1.0, outer strike point), unfolded divertor/PL maps reveal a diagonal, band-shaped wetted area that follows poloidal turns and toroidal drifts. The intensity diminishes toward the high-field side (HFS) where ionization rates decrease. Local maxima occur at protruding surfaces and toroidal leading edges of the divertor, creating a toroidally repeating pattern. NBI-induced PL losses concentrate at the most upstream limiter (PL #3), with progressively reduced loading on downstream PLs. Fig. 4-i illustrates the banded divertor/PL footprint, while Fig. 4-ii shows the leading-edge hot spots and module geometry.

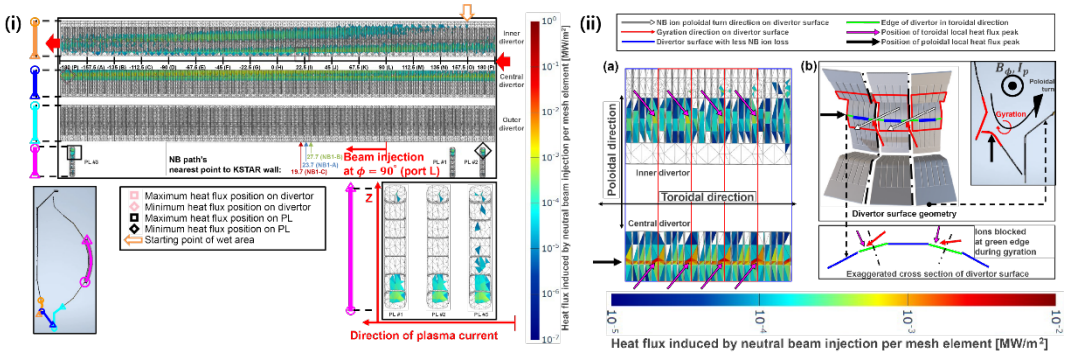

FIG. 4. (i) Heat flux colormap of the unfolded divertor and PL surfaces from the NuBDeC simulation results of the reference setup: 100 keV NB1-C neutral beam for the equilibrium case I in Fig. 3-i. (ii-a) Zoomed-in view of the inner and central

divertor section between 130 and 160 degrees of the toroidal position in (i). (ii-b) The 3D geometry of the inner, central, and outer divertor surfaces. The three areas outlined by red boundaries on the surface correspond to the regions enclosed by the three red rectangles in the center of (ii-a).

3.2. Beam energy and source configuration

Reducing beam energy from 100 to 60 keV narrows the poloidal wetting width and substantially decreases both peak heat flux and total power deposition. This energy reduction yields approximately 75-80% decrease in peak heat flux and 90-95% reduction in deposited power fraction. Among injection geometries, the deposition profile of NB1-C produces the highest losses. The NB1-A source aimed close to core region reduces losses by a factor of 3-4 compared to NB1-C, while NB1-B generates no measurable losses in the tested configurations. These trends are quantified in Fig. 5-7, which present comparative unfolded views and quantitative measurements.

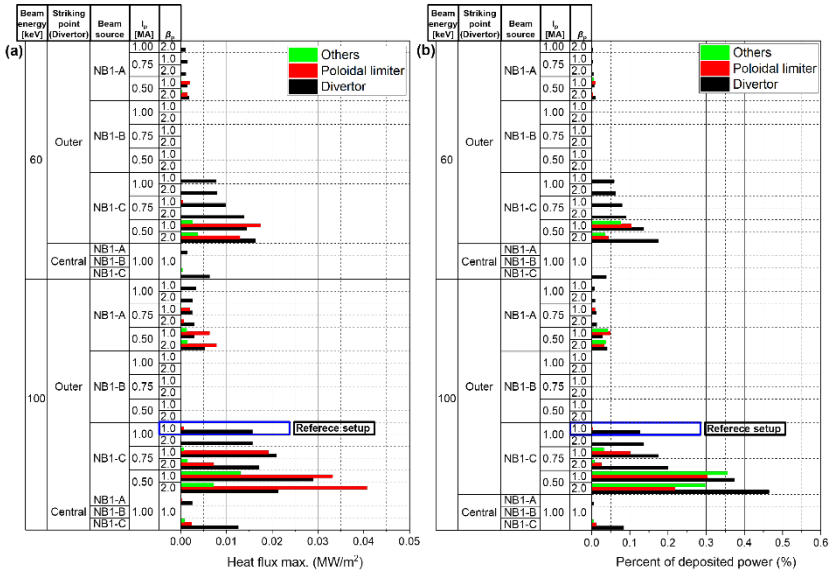

FIG. 5. Maximum heat flux and percentage of power deposition for varying beam energies, beam sources, I_p, β_p, and outer strike point position of the magnetic separatrix on the divertor. The three PFC regions in the legend are illustrated in Fig. 2.

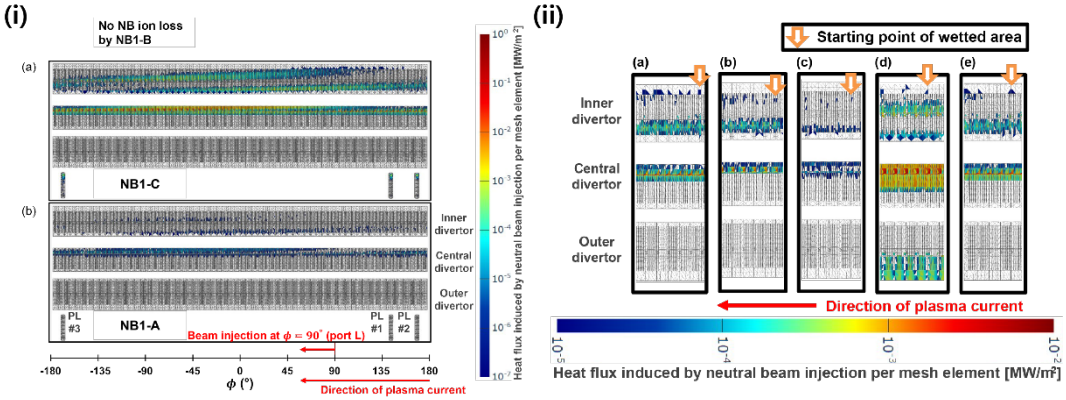

FIG. 6. (i) Variations in beam sources from NuBDeC simulation parameter scans showing (i-a) the reference setup and (i-b) a single-parameter variation to the NB1-A beam source. There is no identified NB ion loss by NB1-B. (ii) Enlarged planar views of the unfolded divertor comparing NuBDeC heat flux distributions due to NB ion loss: (ii-a) reference setup, and single-parameter variations of (ii-b) 60 keV beam energy, (ii-c) NB1-A beam source, (ii-d) I_p= 0.50 MA, and (ii-e) β_p= 2.0. A white arrow with an orange boundary points to the most upstream point in the NB ion trajectories or starting point of the plasma-wetted area.

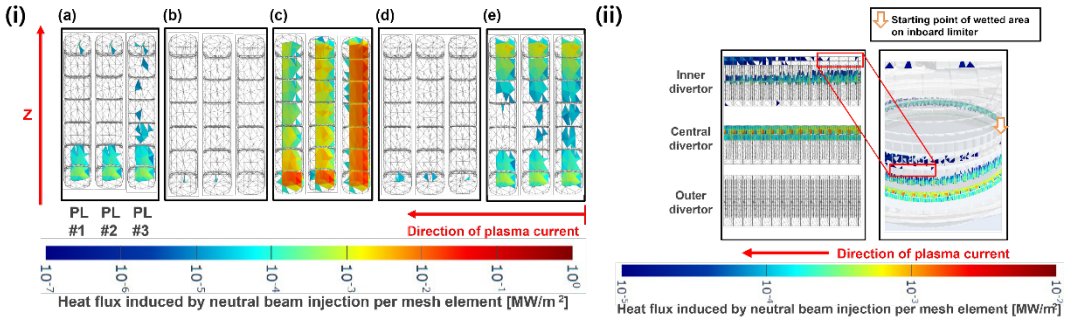

FIG. 7. (i) Enlarged planar views of the unfolded PL comparing NuBDeC heat flux distributions due to NB ion loss: (i-a) reference setup, and single-parameter variations of (i-b) NB1-A beam source, (i-c) I_p = 0.50 MA, (i-d) β_p = 2.0, and (i-e) outer magnetic separatrix strike point on the central divertor. Heat flux on the PL disappears when the beam source is changed from the reference case to a 60 keV NB1-C beam. (ii) Enlarged planar view of the unfolded divertor with the outer strike point of the separatrix positioned on the central divertor, compared to NuBDeC NB ion loss heat flux distributions in Fig. 6-ii. Note that the wetted area reaches the inner limiter. A white arrow with an orange boundary points to the most upstream point in the NB ion trajectories or starting point of the plasma-wetted area.

3.3. Plasma current and poloidal beta effects

Decreasing I_p enhances NBI-induced losses through increased safety factor and amplified radial drift, which broadens the divertor footprint along the poloidal-turn direction and occasionally produces an additional band on the outer divertor. At I_p= 1.00 MA, increasing β_p through the Shafranov shift raises divertor deposition, while at lower I_p values, β_p variation primarily modifies PL loading patterns.

3.4. Strike-point relocation

Relocating the outer strike point from the outer to the central divertor significantly expands the divertor wetted area, enables deposition on the inboard limiter, and shifts PL wetting toward higher Z positions. This edge magnetic field modification produces larger footprint changes than β_p variations and substantially reshapes the heat flux patterns (PL panel in Fig. 7-i-e and Fig. 7-ii). The synopsis corroborates this trend qualitatively.

3.5. Parameter ranges across all scans

Across 42 experimental setups (each with 1 MW NBI input), the observed ranges for regional maxima and power fractions are: divertor heat flux < ~30 kW m^{-2} with power fraction < 0.5%; PL heat flux < ~40 kW m^{-2} with power fraction < 0.3%; other components < ~15 kW m^{-2} with power fraction < 0.35% (Table 2).

TABLE 2. Range of maximum heat flux and percentage of power deposition relative to the total input beam power (1 MW) for each PFC region out of 42 NuBDeC simulation setups using 60/100 keV NB1-A, -B, -C (1 MW of power) across seven magnetic equilibria.

	Divertor	PL	Others
Maximum heat flux [kW/m^2]	< 30	< 40	< 15
Power deposition [%]	< 0.5	< 0.3	< 0.35

4. DISCUSSION

Within the scanned parameter range, this study explains diagonal heat-flux bands, peaks at leading edges (protrusions intercept upstream streamlines), and higher loading on upstream PLs (first interception). Here describes three of the main factors that control the heat flux patterns:

— (Beam deposition location) The poloidal turn orbit and correspondingly the poloidal loss position are presumed to be determined by the beam deposition (i.e., ionization) position. For instance, an ion ionized near the plasma edge proximal to the HFS wall traverses a poloidal turn orbit at a larger minor radius. In this case, its trajectory collides earlier with the PFC surface after a shorter distance from its beam deposition position. In this study, we used beam sources with different tangential radii of beam injection. Notably, when the beam is injected closer to the HFS, the beam deposition also occurs closer to the HFS for the given plasma profiles. Moreover, variations in I_p and β_p lead to changes in the magnetic flux surface, which in turn causes redistribution of the plasma profile and consequently a shift in the beam deposition position.
— (Magnetic geometry shifts) Shifts of the magnetic flux surfaces and the magnetic separatrix's outer strike point cause NB ion losses at different positions, even with identical beam deposition distribution. These geometric modifications alter the intersection points between ion trajectories and material surfaces.
— (Radial drift scaling with safety factor and parallel velocity) Radial drift of NB ions causes a deviation ($\Delta \sim q v_{\parallel}$) of the center of the poloidal turn orbit [6]. $v_{\parallel}$ tends to be higher with increased beam energy. The safety factor increases due to weaker poloidal magnetic field induced by the lower I_p. Therefore, higher beam energy and lower I_p cause the particles to drift more, which results in higher heat flux on divertor.

These mechanisms, which are specifically suggested for the setups of parameter scan range, indicate operational levers;

— The preference for NB1-A-like geometry sources over NB1-C aimed closer to the SOL region when compatible with scenario goals, reducing ion-loss channels.
— The reduction of beam energy when feasible (e.g., from 100 keV to 60 keV), which decreases both maxima (75–80%) and power fraction (90–95%).
— The avoidance of low-I_p/high-β_p combinations that increase drift excursions and broaden wetted areas, particularly during campaign phases with divertor integrity concerns.
— The strategic control of strike-point location between outer and central divertor targets, considering its influence on inboard limiter heat loads due to ion losses.

This use-case demonstrates a systematic approach for quantifying margins and sensitivities of NBI simulation using CAD-geometry model. However, different simulation settings are required when applying this with toroidal non-axisymmetric magnetic field (e.g. RMP), MHD instabilities, or with atomic reactions such as thermalization and charge exchange. These considerations will guide future work to expand the coverage of current methodology.

5. CONCLUSION

NBI heating simulations using NuBDeC code with CAD-based mesh and full-orbit physics predict non-axisymmetric, geometry-sensitive heat flux distribution from NBI-induced ion loss on KSTAR's tungsten PFCs. The distribution form oblique bands with peaks at toroidal leading edges and upstream PLs; ion losses intensify with higher energy, larger β_p, lower I_p, deposition close to SOL region while strike-point relocation strongly reshapes the distribution. Quantitatively, reducing energy from 100 to 60 keV cuts maxima by ~75-80% and power-fraction deposition by ~90-95%; over 42 setups, divertor/PL maxima remain $<$30-40 kW m^{-2} with sub-percent power fractions. These results provide a systematic approach for optimizing NBI configuration to avoid localized hot spots on the W-divertor during future KSTAR campaigns.

These defects are subtle and non-trivial, yet critical to the integrity of larger system operation. The approach can provide a systematic methodology for NBI configuration optimization—identifying conditions where loss is expected and helping to consider if there is any avoidable damage on the wall. Moreover, the resulting heat-flux datasets are visualization-ready in virtual environments such as the V-KSTAR platform and are intended for further use in synthetic diagnostics and integrated simulation, providing engineering-level fidelity and seamless geometrical context on which the data can be mapped.

ACKNOWLEDGEMENTS

This work was supported by the National Research Foundation of Korea (NRF) grant funded by the Korea government (MSIT) (No. RS-2023-00254695). Computing resources were provided on the KFE computer, KAIROS, funded by the Ministry of Science and ICT of the Republic of Korea (KFE-EN2541-11).

REFERENCES

[1] KURKI-SUONIO, T., et al., Protecting ITER walls: fast ion power loads in 3D magnetic field, *Plasma Phys. Control. Fusion* **59** 1 (2016) 014013.

[2] KURKI-SUONIO, T., *et al.*, "Fast particle losses in ITER", 22nd IAEA Fusion Energy Conference (Proc. Int. Conf. Geneva, Switzerland, 2008), International Atomic Energy Agency, Vienna (2008).

[3] WARD, S. H., et al., LOCUST-GPU predictions of fast-ion transport and power loads due to ELM-control coils in ITER, *Nucl. Fusion* **62** 12 (2022) 126014.

[4] KURKI-SUONIO, T., et al., Clearing the road for high-fidelity fast ion simulations in full three dimensions, *J. Plasma Phys.* **84** 6 (2018) 745840603.

[5] AKERS, R., *et al.*, "High fidelity simulations of fast ion power flux driven by 3D field perturbations on ITER", 26th IAEA Fusion Energy Conference (Proc. Int. Conf. Kyoto, Japan, 2016), International Atomic Energy Agency, Vienna (2016).

[6] RHEE, T., et al., Numerical study of neutral beam injection prompt loss at KSTAR poloidal limiters, Phys. Plasmas **26** 11 (2019) 112504.

[7] RHEE, T., et al., Simulation study of fast ion losses associated with the rotating n = 1 resonant magnetic perturbations in KSTAR, *Nucl. Fusion* **62** 6 (2022) 066028.

[8] KIM, K., JHANG, H., KIM, J., RHEE, T., Enhanced fast ion prompt loss due to resonant magnetic perturbations in KSTAR, *Phys. Plasmas* **25** 12 (2018) 122511.

[9] KIM, J. Y., et al., Prompt loss of beam ions in KSTAR plasmas, *AIP Adv.* **6** 10 (2016) 105013.

[10] BAK, J., et al., Measurement of inner wall limiter SOL widths in KSTAR tokamak, *Nucl. Mater. Energy* **12** (2017) 1270–1276.

[11] ÄKÄSLOMPOLO, S., *et al.*, Modelling of NBI ion wall loads in the W7-X stellarator, Nucl. Fusion **58** 8 (2018) 082010.

[12] MOON, T., et al., Development of novel collision detection algorithms for the estimation of fast ion losses in tokamak fusion device, *Comput. Phys. Commun.* **309** (2025) 109490.

[13] WOLF, R. C., *et al.*, Performance of Wendelstein 7-X stellarator plasmas during the first divertor operation phase, Phys. Plasmas **26** 8 (2019)

[14] CORNELISSEN, M. J. H., *et al.*, Identification of fast ion wall loads in Wendelstein 7-X from thermographic measurements, Plasma Phys. Control. Fusion **64** 12 (2022) 125015.

[15] LEVINESS, A., *et al.*, Validation of a synthetic fast ion loss detector model for Wendelstein 7-X, Nucl. Fusion **64** 9 (2024) 096034.

[16] VELARDE, L., *et al.*, Velocity-space analysis of fast-ion losses measured in MAST-U using a high-speed camera in the FILD detector, Plasma Phys. Control. Fusion **67** 1 (2024) 015024.

[17] KWON, J.-M., *et al.*, Progress in digital twin development of virtual tokamak platform, IEEE Trans. Plasma Sci. **52** 9 (2024) 3910–3916.

[18] FRANKE, T., *et al.*, Integration studies of a positive neutral beam injector system into the design of a volumetric neutron source, Fusion Eng. Des. **215** (2025) 115035.

[19] JUAREZ, R., *et al.*, A full and heterogeneous model of the ITER tokamak for comprehensive nuclear analyses, Nat. Energy **6** 2 (2021) 150–157.

[20] JUAREZ, R., *et al.*, ITER full model in MCNP for radiation safety demonstration, Nat. Commun. **15** 1 (2024) 8563.

[21] ERICSON, C., Real-Time Collision Detection, CRC Press, "Boca Raton" (2004).

[22] NA, B., *et al.*, Experimental and numerical evaluation of the neutral beam deposition profile in KSTAR, Fusion Eng. Des. **185** (2022) 113320.